Submitted to ACS Applied Energy Materials, August 2022

High-Mass Loading of Flower-Like Ni-MoS_2 Microspheres Toward Efficient Intercalation Pseudocapacitive Electrode

Sarojini Jeeva Panchu[a], Kumar Raju*[b] Prashant Singh[c], Duane D. Johnson[c,d] and Hendrik C. Swart*[a]

[a]*Department of Physics, University of the Free State, P.O. Box 339, Bloemfontein 9300, South Africa.*

[b]*Energy Centre, Council for Scientific and Industrial Research (CSIR), Pretoria 0001, South Africa.*

[c]*Ames Laboratory, U.S. Department of Energy, Iowa State University, Ames, IA 50011-2416, USA.*

[d]*Department of Materials Science and Engineering, Iowa State University, Ames, IA 50011-1096, USA.*

Abstract:

This work reports the exploration of intercalation pseudocapacitance in a thicker electrode of flower-like Ni-doped MoS_2 microspheres features a mass-loading of ~10 mg/cm^2 without sacrificing the gravimetric capacitance (~425 F/g at 5 mV/s). Integration with Ni atoms in MoS_2 microspheres not only stabilizes the structural integrity but also ameliorates the rapid intercalation and deintercalation of electrolyte ions even at a commercial-level mass loading. The DFT analysis show that reduced number of nano-sheets, responsible for increased capacitance, comes from energy instability introduced by Ni doping that changes the local bonding behaviour and overall electronic-structure of pristine MoS_2. The experiments attribute the overall capacitance enhancement in (Mo-Ni)S_2 increasing the rate of electrolyte ion insertion and extraction , which is confirmed by *b*-values close to 0.5 at different potentials indicating that the current response predominantly depends on the diffusive mechanism for both MoS_2 and Ni-MoS_2 thicker electrodes. The symmetric device constructed with Ni-MoS_2 microspheres exhibited a capacitance value 101 Fg^{-1} in 1 mVs^{-1} of which the energy density is 9 Wh kg^{-1}, as well as attained an outstanding cycling stability of 10,000 cycles with 60% retention at 2 Ag^{-1}. In addition to providing insights into the development of 2D TMDs, this work explores the design of robust and highly efficient intercalation electrode materials for electrochemical energy storage devices.

Keywords

MoS_2, Ni-doped MoS_2, Supercapacitors, Specific Capacitance, 3D microsphere, hydrothermal.

Introduction:

A significant advantages of pseudocapacitors is their superior power density of up to 10000 W/kg, and long lasting performance of more than 20k cycles of pseudocapacitors are particularly promising and have been widely applied in different applications ranging from portable electronics to the automobile sectors[1]. However, the low energy density of supercapacitors (SCs) stems from their further development[2]. Recently, the intercalation pseudocapacitance, which stores energy in the tunnel of bulk electrodes/layers of the active materials through a battery-like intercalation process without altering the crystal phases to efficiently provide a pathway for exploring advanced

SCs exhibiting excellent energy as well as power density[3]. As a family of transition-metal dichalcogenides (TMDCs), which belongs to the group of two dimensional (2D) materials, offers inherent features for intercalation pseudocapacitance owing to their tunable dimensionality nature and layered structures[4,5,6]. The layered 2D MoS_2 with two sulphur atoms that are covalently bonded to from like a sheet and these adjacent sheets are held together by a weak van der Waals (vdWs) force with no dangling bonds offering great flexibility for the intercalation of foreign ions[7]. Supercapacitors' electrochemical performance is improved by the intercalation process, but the overall performance of the device is hampered by the low active mass loading in the majority of the documented literature[8]. A high mass loading is necessary in this regard in order to store enough energy for commercial equipment that runs continuously. Due to insufficient electron and ion transport, the capacity of thicker electrodes with a mass loading of 10–12 mg/cm^2 also degrades quickly. Additionally, the thicker electrode's restricted access to the electrolyte slows down rapid ion transport[9]. In order to prevent substantial deterioration of the capacitance at a large mass loading, it is vital to enable faster reaction kinetics and improve the intake of active materials[10]. 2D layered materials, especially MoS_2 sheets which facilitate the rapid intercalation/deintercalation reactions, making them attractive for electrodes in high energy density aqueous supercapacitors[11]. Conversely, exfoliated nanosheets are in some ways very attractive for supercapacitor electrode materials. The morphology, structure, and particle size of TMDs have also been shown to be key parameters that affect their performance as electrode materials for supercapacitors, despite their lower electrical conductivity than MoS_2[12].

High electronegative Ni^{2+} with an ionic radii of 0.69 Å can easily replace Mo (0.68 Å) atoms in MoS_2 without affecting the hexagonal structure[13] due to the high affinity for bonding with other elements. Additionally, the Ni doping in MoS_2 improves the material's conductivity while also increasing the intrinsic activity of the active sites[14–18]. Ni is a suitable dopant due to its vacant d-orbitals and doping creates multiple oxidation states that results in higher redox reactions and increased pseudocapacitance. The adjacent sulphur atoms presents in doped Ni became the new active sites for SCs[19.] Few research groups have synthesized flower like MoS_2 and its applications as electrode materials for supercapacitors application, however, most of them exhibited the capacitive-controlled behaviours. Zhou et al., synthesized 300 nm diameter flower like MoS_2 by using the hydrothermal method that shows a C_s value of 122 F/g [20]. Chen et al. found a cycling stability of 94.3% over 2000 cycles using a flower-like hybrid of MoS_2/NiCoHC[21].

In this study, the MoS_2 lattice structure was stabilized by doping with an appropriate amount of Ni. This enabled the robust microspheres structure, to improve the rate performance, cycle stability and reaction kinetics of the thicker electrodes by facilitating the high electrolyte accessibility.

Experimental:

Synthesis of Ni-MoS_2:

To prepare MoS_2, 1.95 mmol of $(NH_4)_6Mo_7O_{24}.4H_2O$), 4 mmol of (NH_2CSNH_2) and 0.065 mmol polyethylene glycol (PEG 4000) were mixed in distilled water. The solution mixture was maintained at 200 ºC for 48 h in an autoclave lined out with Teflon. In the preparation of the Ni-MoS_2, $NiCl_2.6H_2O$ was added to the above solution at 1 mmol as an impurity level doping. Before transferring to the autoclave, it was stirred for 3 h to obtain a clear solution. Afterwards a greyish black colour precipitate was collected. The final products were washed with DI-H_2O and anhydrous EtoH and dried under vacuum at 80º C for 12 h.

Material Characterization:

XRD analysis were carried out using a BRUKER-Advance D8-diffractometer (Cu K_α, λ=1.54 Å), in order to determine the phase purity and the crystalline nature of the as synthesized MoS_2 and Ni-MoS_2. The X-ray photoelectron spectroscopy (XPS) measurements were carried out using A PHI 5000 Versaprobe system. The morphological studies were conducted by using a JEOL SEM, model JSM-7800F, operating at a 5 kV accelerating voltage and their corresponding elements were analysed by energy-dispersive spectroscopy (EDS) recorded using a JEOL JSM 6360. A high-resolution transmission electron microscope (HR-TEM) and scanning transmission electron microscope (STEM) measurements were obtained using a JEOL 2100-HRTEM at 200 kV and Oxford X-Max 80 mm SDD (UK) for selected area (electron) diffraction (SAED), STEM and High-angle annular dark-field imaging (HAADF). A copper grid coated with carbon was used for the HR-TEM analyses. Furthermore, optical absorption spectra were acquired using a Perkin Elmer Lambda 950 UV–VIS spectrometer. The Raman analysis was carried out by using a laser Raman (RenishawInvia Raman spectroscopy and microscope) equipped with a He:Ne laser, using an excitation wavelength of 613 nm. Bio-Logic VMP3 @ EC-LAB 10.40 was used for all electrochemical analyses on the MoS_2 and Ni-MoS_2 at room temperature.

Computational method

Projector-augmented wave (PAW)[22] and Perdew-Burke-Ernzerhof (PBE) exchange-correlation[23] were used using density functional theory (DFT), as implemented in Vienna ab-initio Simulation Package[24] (VASP). The optB88-vdw correlation functional was used to include vdWs interactions[25–27]. For Brillouin-zone integrations, a Monkhorst-Pack grid of 1×1×1 k-points was used for the geometrical optimizations of 5×5×1 2H MoS_2 and (Mo-Ni)S_2 supercells, while static calculations were performed on 3×3×3 grids. The energy cutoff for the plane-wave and energy convergence were 520 eV and 1×10^{-6} eV, respectively. The force convergence in geometric relaxation was set to 0.01 eV/Å. The spin-polarized calculation were performed for 2H (Mo-Ni)S_2 to include the effect of ferromagnetism for Ni. The formation energy (E_{form} at 0 K; eV/atom) of 150 atom supercell (see **Figure S4**) was calculated using the standard definition: $E_{form} = [E_{total} - \sum_i n_i E_i]/n$, where E_{total}, E_i, n_i are total energy, elemental energy, and number of atom of each class in the unit cell, respectively[28,29]. The E_{form} was referenced against the most stable elemental phase, i.e., Mo (bcc), S (alpha phase), and Ni (fcc).

Electrochemical measurements

The electrochemical measurements such as cyclic voltammetry (CV) and Electrochemical impedance spectroscopy (EIS) on pristine MoS_2 and Ni-doped MoS_2 were conducted at ambient condition using Bio-Logic VMP3 system. A composite electrode fabricated by coating a slurry containing the active-material 80%, carbon-black 15% with poly (vinylidene fluoride) (PVDF) 5% (weight ratio) on a Ni-foam conductive substrate subsequently vacuum-dried for 12 h at 120°C. A typical 3-electrode setup, the prepared composite electrodes are the working electrode Pt was applied as counter-electrode and Ag/AgCl (KCl) served as a reference-electrode under 1 M Na_2SO_4 aqueous electrolyte. Cyclic voltammograms were performed at potential ranges from -1 to -0.2 V and 0 to -0.8V for half -cell symmetry at various scanning rates of 5 to 100 mVs^{-1}. The EIS measurements were performed by applying the open-circuit voltage with an AC voltage amplitude of 1.5 mV at frequencies of 10 kHz to10 mHz. With Ni-doped MoS_2 electrodes on both sides, a symmetric supercapacitor with two electrodes was created, and it operated within a 1 M Na_2SO_4 aqueous solution as the electrolyte. The following equations were used to compute the specific capacitance (CSP), device capacitance, maximum specific power density (P_{max}), and energy density

(E_{sp}) from the CV and CD curves.

$$C_g = \frac{1}{Vmv}\int i\, dV \tag{1}$$

$$C_{sp}\left(F/g\right) = \frac{4 \cdot C}{m} \tag{2}$$

$$P_{max} = \frac{V^2}{4mR_s} \tag{3}$$

$$E\left(Wh/kg\right) = \frac{CV^2}{2m} \tag{4}$$

where C (F) is the predicted capacitance, V (V) is the maximum voltage reached during charging, and R_s is the corresponding series resistance; i (A) is the applied current; V (V)/ Δt (s) is the slope of the discharge curve; and m (g) is the total mass of both electrodes (ESR). The mass loading of both MoS_2 and Ni-MoS_2 electrodes are ~ 11 and 10.8 mg /cm^2, respectively.

Results and discussion:

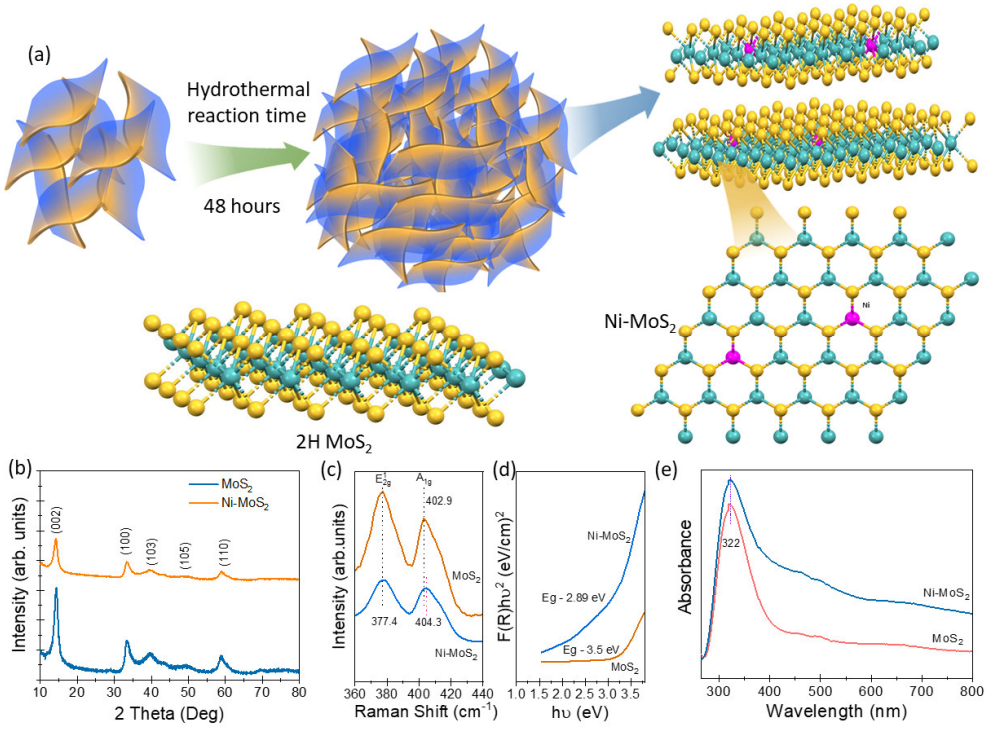

Figure 1. Physico-chemical characteristics of the prepared MoS_2 and Ni-doped MoS_2 microspheres (a) schematic of MoS_2 and Ni-MoS_2 formation via hydrothermal route, and the structures of Ni-MoS_2 and 2H- MoS_2. (b) XRD pattern, (c) Raman analysis (d) Absorption spectral features of MoS_2 and Ni-MoS_2.

In this work, pristine-MoS_2 and Ni-MoS_2 were synthesized using hydrothermal route (**Figure 1(a)**). During the hydrothermal reaction, the reaction takes place between ammonium molybdate and thiourea where the MoO^{4-} and ammonium ions were released from the ammonium molybdate and it reacts with the thiourea to form MoS_2 nanosheets. In general, MoS_2 is likely to form a sheet like structure due to its layered nature. In the spontaneous hydrothermal reaction, unreacted NH_4^+ ions prevent the stacking of nanosheets and vdW force aid to forms interconnected sheets results in a 3D sphere like structure by self-assembly of nanosheets[30]. The size of the nanosheets increases due to the Ostwald ripening process[31]. Upon Ni^{2+} doping in MoS_2 the grain size has increased, compared to the pristine MoS_2. The X-ray diffraction analysis of MoS_2 and Ni-MoS_2 were carried out and Raman spectroscopy was performed for the structural analysis. X-ray Diffraction (XRD) pattern of as-synthesized MoS_2 was compared with Ni-MoS_2 pattern, which is depicted in **Figure 1 (b).** The strong intense peak at 2θ = 14.26° corresponds to the (002) plane representing a well-stacked hexagonal structure and has a d-spacing of 6.2 Å for MoS_2. The diffraction peak at 2θ = 33.58°, 39.64°, 48.3°, 59.18°, and 69.87º corresponds to (100), (103), (105), (110) and (108) planes of 2H-MoS_2, respectively. These crystalline peaks of MoS_2 have been referred to and indexed according to JCPDS file no 75-1539. Due to the very low amount (<5%) of Ni doping, no extra phase was reflected in the Ni-MoS_2 pattern. No additional peak associated with Ni sulphide was identified, which confirms the substitutional incorporation of Ni into the MoS_2. The crystallite size for MoS_2 and Ni-MoS_2 was calculated by using Sherrer equation (1)

$$D = \frac{0.9\lambda}{\beta cos\theta} \quad (1)$$

where D is the crystallite size, λ-wavelength of the X-ray (1.5406 Å), β - is the broadening of the diffraction line measured at half of its maximum intensity, and θ - is the peak position. The crystallite size for MoS_2 was 5.0 nm and for Ni-MoS_2 5.8 nm. Furthermore, the dislocation density (δ) and the strain(ε) values were calculated from the XRD pattern by using equation (2) and (3)

$$\delta = \frac{1}{D^2} \quad (2)$$

$$\varepsilon = \frac{\beta}{4tan\theta} \quad (3)$$

Table 1. Structural parameters of as-synthesized MoS_2 and Ni-MoS_2.

Sample Name	Crystallite size (nm)	Dislocation density	Strain
MoS_2	5.0	18.46 x 10^{15}	0.250
Ni-MoS_2	5.8	22.41 x 10^{15}	0.320

Raman spectroscopy further confirmed the formation of MoS_2 and Ni-MoS_2 (**Figure 1 (c).**) with the vibrational modes of 377.4 and 402.9 cm^{-1} for MoS_2 then 377.4 and 404.3 cm^{-1} for Ni-MoS_2. These are attributed to the peaks from Mo-S and Ni-S bonds. When the Ni is doped in the MoS_2, there was a small shift in the A_{1g} peak towards a higher value.

With the Kubelka-Munk's ($F(R)$) equation, the diffuse reflectance measurements were converted to band gap values. The optical band gap energy is derived from,

$$F(R) = \frac{(1-R)^2}{2\times R} = \frac{k}{s} \qquad (4)$$

where R represents reflectance, k and s are the molar absorption and scattering coefficient.

Kubelka-Munk equation is used to calculate the band gap as follows,

$$[F(R)h\upsilon] = A(h\upsilon - E_g)^n \qquad (5)$$

where A is the proportionality constant, $h\nu$ is the photon energy, $E_g$is the optical band gap, and n is a constant associated with different kinds of electronic transitions (n= 1/2 for a direct allowed, n= 2 for an indirect allowed).

Using a plot of $([F(R)h\nu])^2$ vs $h\nu$, the optical bandgaps of the MoS_2 and Ni-MoS_2 (**Figure 1 (d))** were obtained. MoS_2 has an optical band gap value of 3.25 eV, while Ni-MoS_2 has a bandgap value of 2.89 eV. As a result, the Ni doping of MoS_2 reduced its bandgap value from 3.25 eV to 2.89 eV. Ni doping reduced the bandgap energy of Ni-MoS_2 and increased its electrical conductivity, which resulted in better capacitive properties and higher rate capability.

The optical parameters of MoS_2 and Ni-MoS_2 were analyzed using UV-Vis Spectra. From UV-Vis spectra, it is evident that MoS_2 and Ni-MoS_2 exhibit strong absorption in the wavelength range of 250-800 nm (**Figure 1 (e).**). It shows the characteristics of a strong absorption band at 322 nm. Upon Ni doping, the optical absorption increased towards a higher wavelength which is attributed to the quantum confinement (slightly larger size) and edge effect.

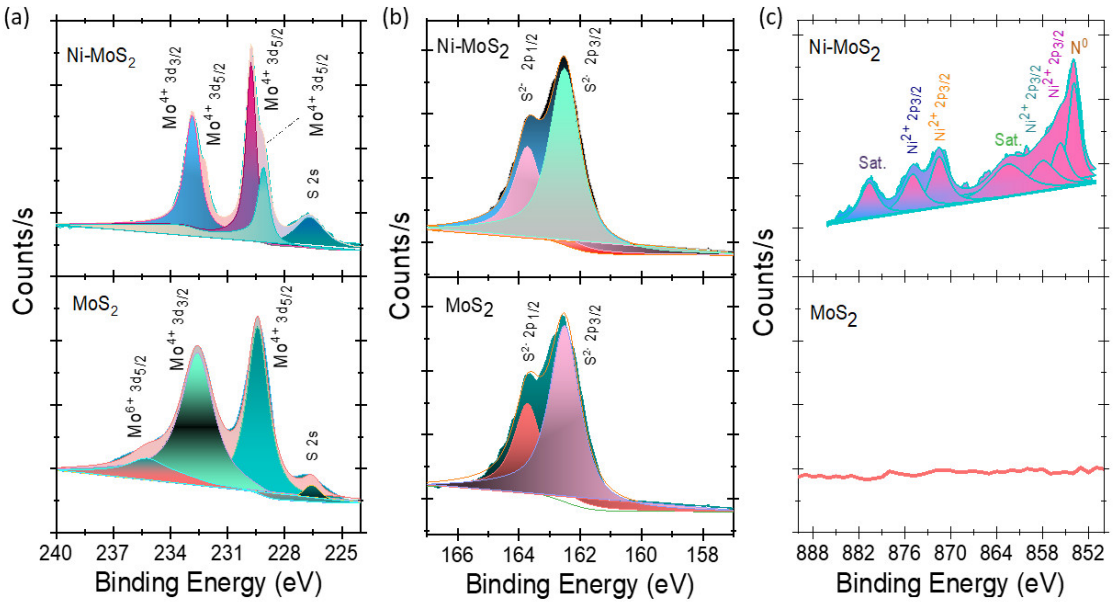

Figure 2. XPS spectra of (a) Mo (b) S of MoS_2 and Ni-$MoS_2$and (c) Ni of Ni-MoS_2.

The chemical oxidation states of MoS_2 and Ni-MoS_2 were analyzed using XPS. Ni-MoS_2's survey spectrum illustrates traces of Mo, S, Ni, C, and O (**Figure S1**). The Mo 3d and S 2p of both the MoS_2 and Ni-MoS_2 were fitted using two doublets. The Mo maxima were centred at binding energys (BEs) of 232.5 and 229.4 eV for the MoS_2 and at 232.9 eV and 229.8 eV for the Ni-MoS_2. These correspond to Mo^{4+} of the hexagonal MoS_2 phase. It is affirmed that the Mo element was mainly present in Mo (IV) in MoS_2. Based on changes in the electronic structure of molybdenum because of N incorporation, the MoS_2 component of the Mo 3d peak exhibited a 0.4 eV shift toward lower BEs with respect to the pure sample (**Figure 2 (a))** [34]**.** Thus, Ni doping increased the electron-rich surface which has a direct effect on the electrocatalytic activity of MoS_2. The peak at 226. 7 eV is defined by S 2s. The S 2p peaks were fitted with a dual component at 162.5 and 163.7 eV for MoS_2 and for Ni-MoS_2 corresponding to S $2p_{3/2}$ and S $2p_{1/2}$ of MoS_2 and these values are in line with literature reports (**Figure 2 (b)**).

Furthermore, the Ni 2p peak was deconvoluted into chemically shifted components to identify the Ni species. Two resolved double peaks resultant to Ni $2p_{3/2}$ and $2p_{1/2}$ with a difference of 17.5 eV and two satellites are observed at the Ni 2p spectrum. The BE value at 855.4 eV, 857.7 and 871.4, and 874.8 eV are corresponding to Ni $2p_{3/2}$ and Ni $2p_{1/2}$ states (Ni^{2+}) as shown in **Figure 2 (c)**. The BE value at 855.4 eV is attributed to the Ni-Mo-S structure[32]. The peak at 853.9 eV corresponds to the metallic Ni state.

The field-emission scanning electron microscope (FE-SEM) was employed for the analysis of particle size and microstructure of MoS_2 and Ni-MoS_2 as shown in **Figure 3**.

Figure 3 ((a) and (b)) illustrates various magnifications of a MoS_2 microsphere with a flower-like morphology with a size of ~ 1.2 μm which consisting of ~260 nm nanosheets and the thickness of each nanosheet was ~14 nm. As a nature of layered structure, the MoS_2 nanosheets were interconnected and self-assembled into a microsphere. When the MoS_2 was doped with Ni, the size of the microspheres have increased (~ 4 μm) which consisting of ~684 nm nanosheets with a thickness of ~ 18 nm. The increased grain size upon doping resulted in an increase in the size and structure of the Ni-MoS_2 microspheres. As a result of the reaction process, these tiny nanosheets were inter-crossed by being bent, curled, and entwined to form a flower-like structure on the surface of the microspheres. It is evident from **Figures 3 ((c) and (f))** at higher magnification, that the flower-like structure consisted out of tiny nanosheets with a thickness of a few nanometers (<20 nm). There was a significant difference at the edges of the microsphere formed by MoS_2 and Ni-MoS_2 and this have a significant impact on the charge storage and ion intercalation process at the electrode and electrolyte interface.

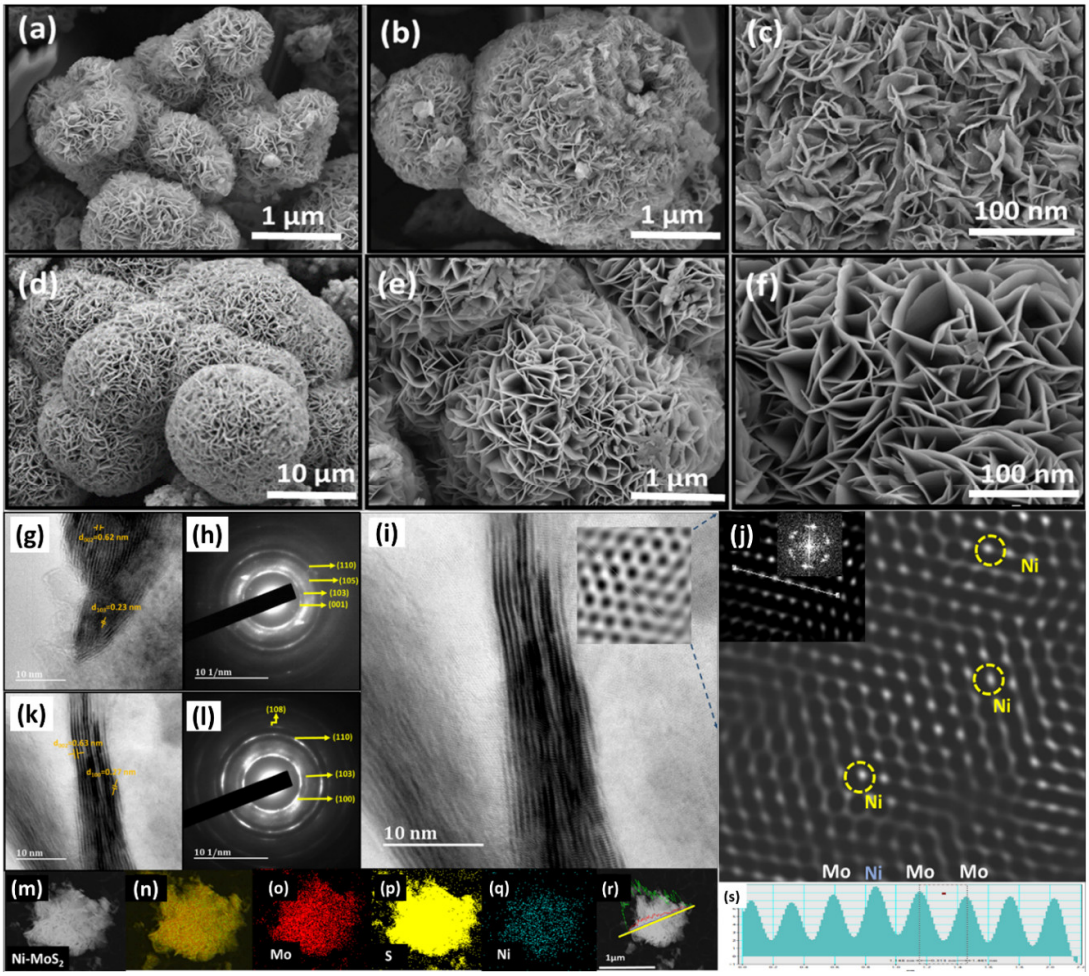

Figure 3. FE-SEM images of flower like MoS_2 ((a)-(c)) and Ni-MoS_2 ((d)-(f)). HR-TEM image of MoS_2 (g), Ni-MoS_2 (k) at high-magnification, and their corresponding SAED pattern of MoS_2 (h) and Ni-MoS_2 (l). Elemental distribution analysis of Ni-MoS_2 flower like microsphere recorded by aberration-corrected HAADF-STEM (m) with composite elemental mapping (n) of Mo(o), S(p), and Ni (q) and line-mapping of Ni-MoS_2 (r). Fourier-filtered image for presenting a better view of the lattice structure and it presents the atomic configuration of Mo and S of MoS_2 (i), Line-profile outlined in (j) and it illustrates the d-spacing value of 0.319 nm (s).

EDS analysis was performed to confirm the elements present in MoS_2 and Ni-MoS_2 (**Figure S1 and S2**), and the presence of the Mo, S, and Ni elements were depicts. In addition, the elemental distribution of Ni, Mo, and S was explained using the elemental mapping. The presence of the Ni atom in Ni-MoS_2 was confirmed by EDS and the elemental map analysis confirmed the Ni atoms were homogeneous successfully doped in the MoS_2. The HR-TEM was employed to obtain deeper understanding of the MoS_2 and Ni-MoS_2 microstructure (**Figure S3**). From the HR-TEM images, the as-grown MoS_2 (**Figure S3 (a) and (b))** and Ni-MoS_2 (**Figure S3 (c) and (d))** showed a flower-like hierarchical microsphere composed of petal-like nanosheets. The stacked nanosheets are extended out on the edges of the microsphere which formed together as a flower-like structure. The

flower-like architecture contained a few layers of nanosheets that possessed a higher surface area which provided the percolation of the electrolyte for a better electrode-electrolyte interface in terms of supercapacitor applications. At higher magnification of the MoS_2 and Ni-MoS_2 in **Figure 3 (a) and (b)**, the few-layered nanosheets from the microsphere contained approximately 25 layer for the MoS_2 while it contained approximately 10 layers for the Ni-MoS_2.

In **Figure 3 (g)** the d-spacing of 0.62 nm and 0.23 nm are in accordance to the (002) and (103) phases of MoS_2, and for Ni-MoS_2 in **Figure 3, (k)** the d-spacing values are measured to be 0.63 nm and 0.27 nm in accordance with the (002) and (100) phase of MoS_2. The fringe patterns are the reflection of Moïre patterns that formed by overlapping two different phases that arise from the MoS_2. Compared to MoS_2 the Ni-MoS_2 shows fewer layers formed due to the doping of Ni. The corresponding SAED pattern for MoS_2 and Ni-MoS_2 are shown in **Figure 3 (h) and (l)**, which reflects the phases of (001), (103), and (110) that well correlates with the XRD analysis.

From **Figure 3 (i)** the higher magnified single layer of the Ni-MoS_2 layer is observed. The Fourier-filtered image corresponding to **Figure 3 (j)** gives a more comprehensive understanding of the lattice structure of the Ni-MoS_2. The Ni atoms are brighter in comparison with the Mo atoms and it confirmed that the Ni dopants occupied the Mo sites in the Ni-MoS_2. The lattice constant value of 0.319 nm (Mo-Mo) has been derived using line profiles in the Ni-MoS_2 crystal (**Figure 3 (s)**). MoS_2 is distorted and its electronic structure is modified due to the selective occupancy of Ni dopants in the basal planes, influencing its catalytic properties[33]. In MoS_2, the Ni doping lead to multiple oxidation states and reversible redox reactions. In Ni-MoS_2, the conductivity has been increased as well as Ni and Mo exhibit corrosion resistance at the electrode-electrolyte interface[34]. As a layered material gets closer to being a single layer in thickness, its properties are determined by that thickness. The activation of the thermodynamically favoured basal planes would have significant advantages in improving the electrocatalytic activity of MoS_2 and nearly all their surfaces would be exposed to the electrolyte. The inactive surface of MoS_2 is activated when metal nanoparticles are incorporated into the basal planes. Additionally, the Ni modification on basal sites would explain the relatively larger number of basal sites compared with edges[35]. Adding Ni atoms reduced the number of layers, resulting in more active sites available for enhancing the electrocatalytic activity of Ni-MoS_2.

A high annular dark field (HAADF) scanning tunnelling electron microscopy (STEM) and EDS mapping were employed for the MoS_2 and Ni-MoS_2. **Figure 3 (m)** shows the morphology of the Ni-MoS_2 using HAADF imaging. The 3D-flower like MoS_2 formation from the interconnected nanosheets are visible. The elemental distribution over the single flower like microsphere was

investigated by using STEM/EDS for Ni-MoS_2 **(Figure 3 (n))**. The Mo, S, and Ni distribution over the single Ni-MoS_2 that reveals the insertion of Ni atoms and its homogeneous elemental distribution over the flower like microstructure were confirmed by elemental mapping (**Figure 3 (o-q)**) and the line mapping (**Figure 3 (r)**).

Theory results and discussion: Thermodynamic stability of novel materials can be used to direct synthesis. The formation enthalpy (E_{form} at 0K) plot for 2H-($Mo_{1-x}Ni_x$) S_2, x= 0-10 at.% (n=0-5 atoms) is shown in **Figure 4 (a)**, where substitutional Ni doping positively increases the E_{form} with respect to 2H MoS_2. In order to comprehend the experimental finding that 1 at.%Ni substitutes to 2H-MoS_2, we compared the electrical structures of the cases with and without Ni doping. (choosing 2 at.%Ni in our numerical calculations to minimize the supercells size and computational time). In **Figure 4 (b-d)**, the total and partial electronic density of states (PDOS) of pristine and Ni substituted 2H-MoS_2 are plotted. The 2H-MoS_2 PDOS in **Figure 4(c)** suggests that the valence bands are mainly from Mo-*4d* states, while the conduction bands Mo-*4d* and S-*3p* states. However, Ni-doped PDOS in **Figure 4(d)** shows gap states near E_{Fermi} are generated by the interplay of Mo-*4d*, Ni-*3d,* and S-*3p* bands with a formation energy of 30 meV-atom^{-1} higher than in the pristine case, see **Figure S5**. The Mo-4*d* and S-3*p* states shift close to the valence band minimum near -0.25 eV below E_{Fermi}. The gap states are found both at valence and conduction band edges near E_{Fermi} in **Figure 4(b)**. These states originate from a crystal field created by the trigonal prismatic structure of Ni/Mo-S. Furthermore, small partially-filled states and peaks in the gap region originate from the mixture of S-*3p* bands with Ni-3*d* and Mo-4*d* states. Notably, the contribution of these bands in **Figure 4(b)** is weak. **Figure 4(b-d)** shows weak gap states and a reduced bandgap, both of which point to improved conductivity in Ni-doped 2H-MoS_2 relative to pristine levels of Ni lead electron donating[36]. This suggests that the electron doping can be used in an efficient way to create gap states, which also has created induced magnetic moments both at Mo and S sites in 2H-MoS_2. The substitutional Ni doping may also be useful for spintronic applications. The reduced energy stability of the Ni-doped case in **Figure 4(a)** can be connected to partially filled peaks at/near the Fermi-level that are known to destabilize the crystalline phases[29].

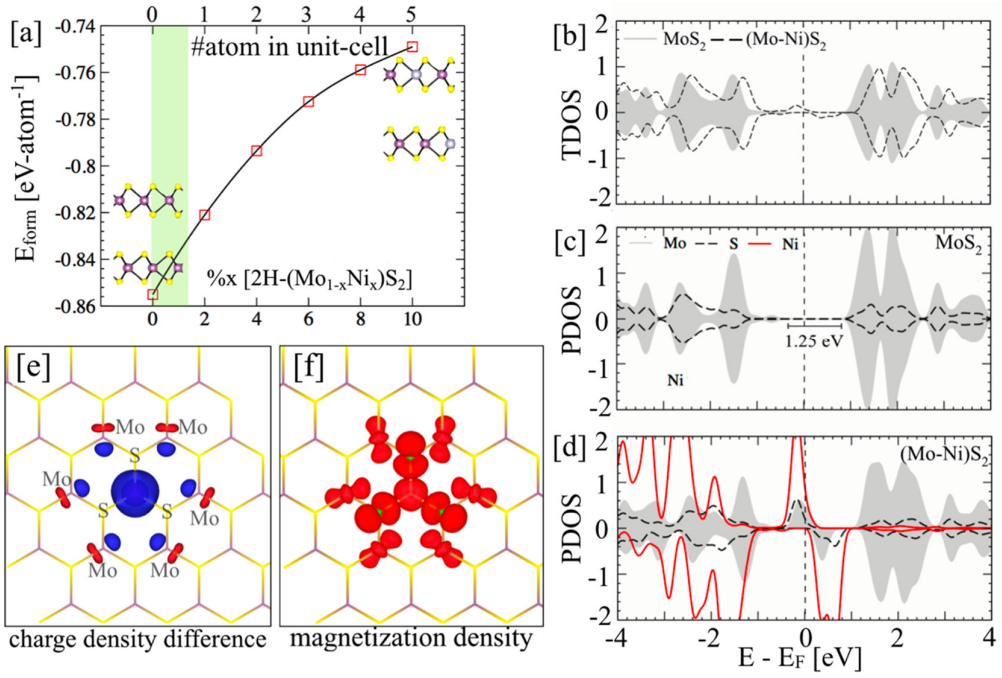

Figure 4. (a) Formation enthalpy (E_{form}; eV/atom) of substitutionally-doped 2H-MoS_2 with Ni, where x-axis present both Ni at.% and equivalent atom numbers in the supercell (Fig. S1). (b) Total, and (c, d) partial density of states (DOS) of pristine and Ni-doped 2H-MoS_2. DOS is in unit of States-eV^{-1}-$atom^{-1}$. Ni PDOS was not scaled for better view. (e) Charge-density difference ($\Delta\rho\ (MoS_2 - (Mo - Ni)S_2)$), and (g) magnetization-density plot for 2H-MoS_2. The isosurface value of 0.02 eV/Å were used for both the charge and magnetization density plots.

Understanding bonding behavior and the underlying cause for the alteration in stability of crystalline materials requires knowledge of the electron and magnetization densities. The chare-density difference $\Delta\rho\ (MoS_2 - (Mo - Ni)S_2)$ between pristine and Ni substituted 5×5×1 supercell is shown in **Figure 4(f)**, where blue lobes are charge gain (by Mo), while red lobes are charge lost (by Ni). The Ni substitution induces strong charge sharing near doped Mo/S sites, which is reflected through reduced bond lengths (stronger bonds) of Ni with its neighbouring atoms. The Mo polyhedral away from Ni sites shows similar bond lengths as in pristine 2H-MoS_2, i.e., 2.416 Å, while doped cases show varying Mo-S (2.407 and 2.418 Å) and Ni-S (2.412 Å) bond lengths in **Figure 4(f)**. However, we found negligible overall volume change (ΔV~0.1 $Å^3$) in Ni substituted 2H-MoS_2 concerning pristine MoS_2, which is possible because of weak Ni concentration (~2 at.%Ni or 1 atom per cell). This bond asymmetry and smaller Ni-S bond lengths are suggestive of strong covalent Ni-S bonding, and Mo-S bond lengths in Ni-doped case are nearly 0.5% smaller compared to pristine 2H-MoS_2.

In **Figure S6**, the maxima in the 2D charge-density contour plot in Ni-S basal plane are slightly smaller than Mo-S. This difference arises from increased bond distortion (0.2 Å) in 2H-(Mo-Ni)S_2,

while no such distortion was observed in Mo-S bond lengths away from the Ni neighbourhood. The reduced phase stability in **Figure 4(a)**, and increased local bonding in **Figure 4(e,f)** for 2H-(Mo-Ni)S_2 explain the reduced number of nanosheets (12-15) compared to pristine 2H-MoS_2 (20 nanosheets). The magnetization density plot in **Figure 4(f)** shows induced magnetic moments both on Mo and S sites, which arise from increased charge activity due to the substitutional doping of Ni at Mo sites.

Electrochemical Performance

Electrochemical performance of flower-like MoS_2 and Ni-MoS_2 electrodes have been investigated in a half-cell configuration using a 1M Na_2SO_4 aqueous electrolyte. **Figure 5(a)** depicts the cyclic voltammetric (CV) evolution for both MoS_2 and Ni-MoS_2 samples with sweep rate ranging from 5-30 mVs^{-1} at the potential range of -1 to -0.2 V. In both MoS_2 and Ni-MoS_2, the CV curves are near rectangular, but defects at Ni-MoS_2 owing to exposed edge-sites increase the dangling edge's active sites for faradic redox reactions. Furthermore, the edge-terminated size of Ni-MoS_2 could provide an ample exposure for the intercalation of electrolyte ions coupled in confined paths that has shorten diffusion length contributes significantly to current response than the pristine MoS_2. It is noteworthy that the Ni-MoS_2 rectangular CV curve's deviation shows a strong corelation with the diffusive process. The defects induced structure-property relationship of Ni -MoS_2 may effectively participate in the enhancement of specific capacitance reaches 425 F/g at 5 mV/s (~367 F/g from pristine MoS_2) whereas it retains the initial capacitance of 92 F/g even in the higher scan rate of 100 mV/s (85 F/g for MoS_2), indicating that the Ni doping enhanced the rate capability.

The EIS analysis has further confirmed the larger ion propagations in Ni-MoS_2 than the pristine MoS_2 by showing the lower contact resistance (R_s) and charge-transfer resistance (R_{ct}). An anlysis of Nyquist's plot for both electrodes (**Figure 5(c)**) in a half-cell configuration demonstrated that the Ni-MoS_2 exhibits a low R_s and R_{ct} values of 2.7Ω and 3.68Ω respectively (R_s of 3.2Ω and R_{ct} of 4.27 Ω for pristine MoS_2) with a deviated vertical curve at low-frequency region of Nyquist plot due to the diffusion of electrolyte ions which is of typical supercapacitor behaviour. These results indicate that Ni-MoS_2 has an improved electrical conductivity and red-ox kinetics.

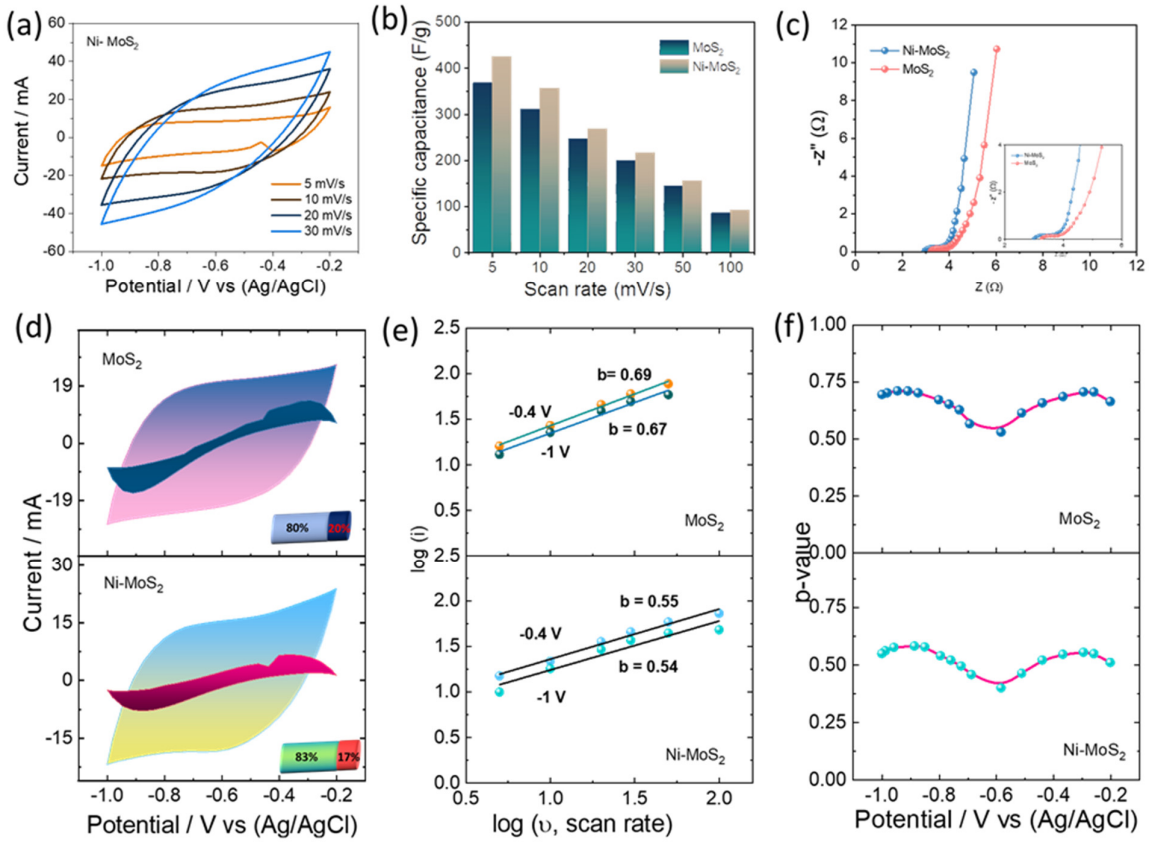

Figure 5. Electrochemical characteristics of flower-like MoS_2 and Ni-MoS_2 analyzed in a three-electrode setup containing a 1 M Na_2SO_4 aqueous solution. (a) CVs of Ni-MoS_2 at various scan rates, (b) determined specific capacitance values based on the different scan rates. (c) Nyquist plot analyzed by EIS. (d) CVs of MoS_2 and Ni-MoS_2 on a scan rate of 10 mV/s, capacitive-controlled process are indicated by shading. (e) the *b* values of MoS_2 and Ni-MoS_2 for various sweep rates, (f) the variation of *b*-values as a function of potentials.

The total charge in flower-like MoS_2 and Ni-MoS_2 was quantified by evaluating (i) capacitive-controlled and (ii) diffusion-controlled faradaic contribution [37]. These contributions might be separated by applying the power-law relationship with measured current (i) with respect to sweep rate (υ) from CV.

$$i = a\upsilon^{b} \qquad (4)$$

where “a” and “b” are adjustable parameters. Generally, a slope value of "b" indicates the dominant contribution; if b=0.5 for a diffusion-controlled and b =1 for the capacitive process. **Figure (e) and (f)** indicate that the as-designed flower-like MoS_2 and Ni-doped MoS_2 show close enough b-values at different potentials like b = 0.67 at -0.1V and 0.69 at -0.4 V and b = 0.54 at -0.1V and 0.55 at -0.4 V, Hence, the current response is significantly owing to diffusive mechanisms for both MoS_2 and Ni-MoS_2 electrodes. By the b -values, the enhancement of the overall capacitance of Ni-MoS_2

is mainly attributed to the rapid insertion and extraction of electrolyte ions. The capacitive contribution to the overall current response can be separated by

$$i\,(V) = k_1\upsilon + k_2\upsilon^{1/2} \quad (5)$$

where υ is the scan rate (mV/s), $k_1\upsilon$ and $k_2\upsilon^{1/2}$ are the currents related to capacitive contribution and diffusion-controlled faradaic contribution, respectively.

$$\frac{i\,(V)}{\upsilon^{\frac{1}{2}}} = k_1\upsilon^{1/2} + k_2 \quad (6)$$

Equations 5 and 6 can be changed to produce a linear plot, and k_1 and k_2 can be computed from $i(V)/\upsilon^{1/2}$ versus $\upsilon^{1/2}$ with various scan rates.

The CV profile of Ni-doped and flower-like MoS_2 at a 10 ms^{-1} scan rate is shown in **Figure 5(d)**. The influence of the capacitive-controlled process is seen by the shaded areas. The intercalation process, which is controlled by diffusion and accounts for 83% (80 for MoS_2) of the Ni-doped MoS_2's flower-like design, adds to the material's overall capacitance. Due to the interaction between Ni and S, which results in lattice distortions and changes in local electronic structures, the intercalation process increases, showing that the electrodes have higher redox activity. This interaction also results in a reduction in the number of layers in Ni-doped 2H-MoS2, which exposes more active sites for the intercalation of ions. This rapid ion insertion and exertion phenomena in a symmetric cell is demonstrated schematically in **Fig.6a.**

Figure 6(b) shows the CV characteristics of the symmetric device of the Ni-MoS_2 in 1 M Na_2SO_4 aqueous solution at different scan rates ranging from 5 to 50 mV/s. As excepted, the CV characteristics exhibited a higher current response with the voltage window of 0 - 0.8 V which is optimized in the three-electrode system. The higher current response of Ni-doped MoS_2 can again be obtained from the enhanced intercalation activity of electrolyte ions.

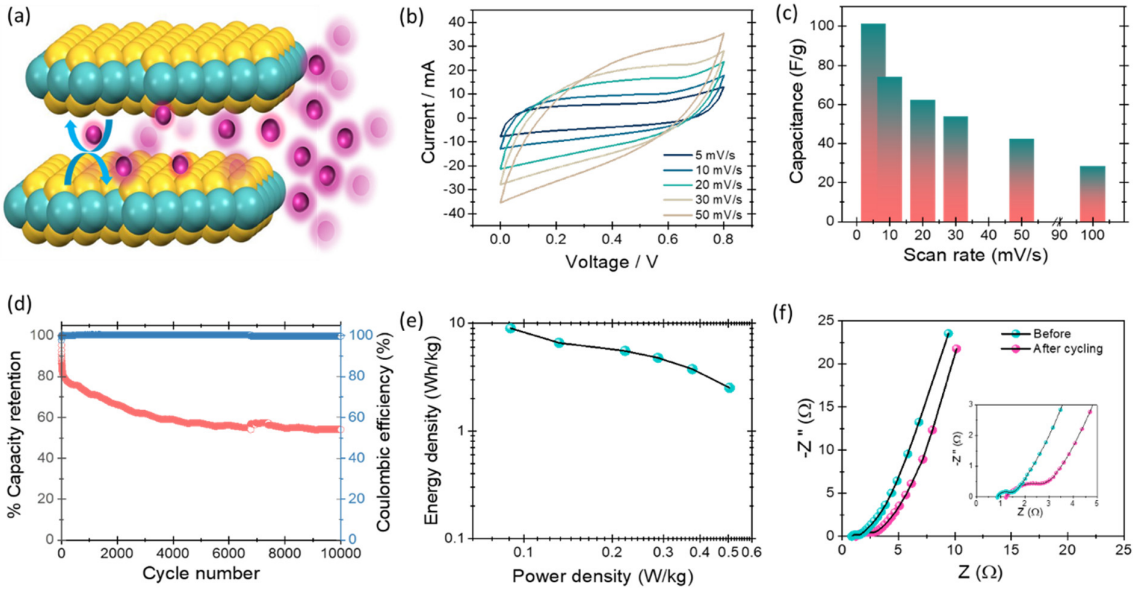

Figure 6. Electrochemical performance of a symmetric aqueous supercapacitor in a 1 M Na_2SO_4 aqueous solution. (a) Schematic of the ion transport mechanism in MoS_2 layers (b) CV curves of symmetric device for Ni-MoS_2, (c) Device capacitance calculated from the CVs recorded at various scan rates, (d) Cycling stability test of the Ni-MoS_2 symmetric device at a current density of 2 A/g, (e) Ragone profile for energy and power density of the device, (f) Nyquist profile for Ni-MoS_2 and Ni-MoS_2 tested after 10000 consecutive cycles, (inset: An enlarged view of the Nyquist plot).

Incorporating Ni atoms into the MoS_2 lattice with an increase in edge atoms and hierarchically built 2D nanoflowers with shorter conductive routes results in surface defects that are close enough to ensure that ion intercalation substantially controls the redox kinetics and surface reactions. The Ni-MoS_2 based device exhibited an initial capacitance of 101 F/g, the CV response (**Figure 6 (c)**) displays outstanding rate capability and retained around 23% (28.3 F/g) of its starting capacitance at a higher scan rate of 100 mVs^{-1}. The cycling stability test was conducted on a Ni-MoS_2 symmetric device with 10000 consecutive cycles at 2 A/g, suggests a comparable cycle life with the capacitance retention of ~ 60% with 100 % coulombic efficiency (**Figure 6 (d)**). It is further evident from the EIS analysis that the observed low R_s and R_{ct} values of 0.89 and 1.56 Ω of the Ni-MoS_2 symmetric device infer the excellent rate capability (**Figure 6 (e)**). The symmetric device achieved a higher energy density of 9 Wh/kg and a power density of 0.5 W/kg (**Figure 6 (e)**). The cycling stability and resistance gain of Ni-MoS_2 was further validated by EIS analysis following a continuous charge-discharge cycles, exhibited nearly linear curves indicating minimal resistance rise (**Figure 6 (f)**), providing proof of the material stability of Ni-doped MoS_2.

Conclusion:

The Ni dopant occupied the interstitial Mo sites in the Ni-MoS_2. The synergistic effect among the Ni-S creates distortion in the lattices along with a change in local electronic structures, this results in an increase in the basal plane activation by reducing the layer numbers in Ni-doped 2H-MoS_2, thus exposed more effective locations for ion intercalation. Our DFT analysis showed that a reduced number of 2H-MoS_2 layers originated from the energy instability introduced by Ni substitution. Notably, the change in the energy instability of the Ni-doped 2H-MoS_2 came from the change in local charge sharing between the Ni and the neighbouring Mo/S sites, which was reflected in a changed electronic-structure. The reduced phase stability and increased local bonding in 2H-(Mo-Ni)S_2 explains the reduced number of nanosheets (12-15) compared to pristine 2H-MoS_2 (20 nanosheets). We also demonstrated that the designing of Ni doped 3D microflowers of MoS_2 potentially offers a number of electrochemically active sites, enabling faster reaction kinetics, even at a mass loading of 10 mg/cm^2. These findings could provide new insights into various physicochemical properties in stacked TMDCs and helped in the development of durable and energy-efficient intercalation electrode materials for high energy density supercapacitors, electrocatalysts, and batteries.

Author Contributions

All authors contributed to the manuscript and discussed the findings and approved the final manuscript.

Notes

The authors declare no competing financial interest.

Acknowledgement

The authors gratefully acknowledge the South African Research Chairs Initiative (SARChI) of the Department of Science and Technology and the National Research Foundation of South Africa (84415). The financial support from the University of the Free State, South Africa is highly appreciated. The work at Ames Laboratory was supported by U.S. Department of Energy (DOE), Office of Science, Basic Energy Sciences, Materials Science & Engineering Division. Ames Laboratory operated by Iowa State University for the U.S. DOE under contract DE-AC02-07CH11358.

References

(1) Chang, L.; Hu, Y. H. Breakthroughs in Designing Commercial-Level Mass-Loading Graphene Electrodes for Electrochemical Double-Layer Capacitors. *Matter* **2019**, *1* (3), 596–620. https://doi.org/10.1016/j.matt.2019.06.016.

(2) Gogotsi, Y.; Simon, P. True Performance Metrics in Electrochemical Energy Storage. *Science (80).* **2011**, *334* (6058), 917–918. https://doi.org/10.1126/science.1213003.

(3) Liu, Y.; Jiang, S. P.; Shao, Z. Intercalation Pseudocapacitance in Electrochemical Energy Storage: Recent Advances in Fundamental Understanding and Materials Development. *Mater. Today Adv.* **2020**, *7*, 100072. https://doi.org/10.1016/j.mtadv.2020.100072.

(4) Joseph, N.; Shafi, P. M.; Bose, A. C. Recent Advances in 2D-MoS_2 and Its Composite Nanostructures for Supercapacitor Electrode Application. *Energy & Fuels* **2020**, *34* (6), 6558–6597. https://doi.org/10.1021/acs.energyfuels.0c00430.

(5) Choi, W.; Choudhary, N.; Han, G. H.; Park, J.; Akinwande, D.; Lee, Y. H. Recent Development of Two-Dimensional Transition Metal Dichalcogenides and Their Applications. *Mater. Today* **2017**, *20* (3), 116–130. https://doi.org/10.1016/j.mattod.2016.10.002.

(6) Cherusseri, J.; Choudhary, N.; Sambath Kumar, K.; Jung, Y.; Thomas, J. Recent Trends in Transition Metal Dichalcogenide Based Supercapacitor Electrodes. *Nanoscale Horizons* **2019**, *4* (4), 840–858. https://doi.org/10.1039/C9NH00152B.

(7) Yoo, H. D.; Li, Y.; Liang, Y.; Lan, Y.; Wang, F.; Yao, Y. Intercalation Pseudocapacitance of Exfoliated Molybdenum Disulfide for Ultrafast Energy Storage. *ChemNanoMat* **2016**, *2* (7), 688–691. https://doi.org/10.1002/cnma.201600117.

(8) Ma, K.; Liu, Y.; Jiang, H.; Hu, Y.; Si, R.; Liu, H.; Li, C. Multivalence-Ion Intercalation Enables Ultrahigh 1T Phase MoS_2 Nanoflowers to Enhanced Sodium-Storage Performance. *CCS Chem.* **2021**, *3* (5), 1472–1482. https://doi.org/10.31635/ccschem.020.202000323.

(9) Yuxiang Wen, Yanpeng Liu, Ting Wang, Zilei Wang, Yanan Zhang, Xiaogang Wu, Xueting Chen, Shanglong Peng, and D. H. High-Mass-Loading Ni−Co−S Electrodes with Unfading Electrochemical Performance for Supercapacitors. *ACS Appl. Energy Mater.* **2021**, *4* (7), 6531–6541. https://doi.org/10.1021/acsaem.1c0055.

(10) Yang, J.; Lian, L.; Ruan, H.; Xie, F.; Wei, M. Nanostructured Porous MnO_2 on Ni Foam Substrate with a High Mass Loading via a CV Electrodeposition Route for Supercapacitor Application. *Electrochim. Acta* **2014**, *136*, 189–194. https://doi.org/10.1016/j.electacta.2014.05.074.

(11) Sarkar, D.; Das, D.; Das, S.; Kumar, A.; Patil, S.; Nanda, K. K.; Sarma, D. D.; Shukla, A. Expanding Interlayer Spacing in MoS_2 for Realizing an Advanced Supercapacitor. *ACS Energy Lett.* **2019**, *4* (7), 1602–1609. https://doi.org/10.1021/acsenergylett.9b00983.

(12) Chhowalla, M.; Shin, H. S.; Eda, G.; Li, L.-J.; Loh, K. P.; Zhang, H. The Chemistry of Two-Dimensional Layered Transition Metal Dichalcogenide Nanosheets. *Nat. Chem.* **2013**, *5* (4), 263–275. https://doi.org/10.1038/nchem.1589.

(13) Ali, M. Y.; Khan, M. K. R.; Karim, A. M. M. T.; Rahman, M. M.; Kamruzzaman, M. Effect of Ni Doping on Structure, Morphology and Opto-Transport Properties of Spray Pyrolised ZnO Nano-Fiber. *Heliyon* **2020**, *6* (3), e03588. https://doi.org/10.1016/j.heliyon.2020.e03588.

(14) Zhang, D.; Wu, J.; Li, P.; Cao, Y. Room-Temperature SO_2 Gas-Sensing Properties Based on a Metal-Doped MoS_2 Nanoflower: An Experimental and Density Functional Theory Investigation. *J. Mater. Chem. A* **2017**, *5* (39), 20666–20677. https://doi.org/10.1039/c7ta07001b.

(15) Dong, T.; Zhang, X.; Wang, P.; Chen, H. S.; Yang, P. Formation of Ni-Doped MoS_2 Nanosheets on N-Doped Carbon Nanotubes towards Superior Hydrogen Evolution. *Electrochim. Acta* **2020**, *338*, 135885. https://doi.org/10.1016/j.electacta.2020.135885.

(16) Chang, Z.; Ju, X.; Guo, P.; Zhu, X.; Liao, C.; Zong, Y.; Li, X.; Zheng, X. Enhanced Performance of Supercapacitor Electrode Materials Based on Hierarchical Hollow Flowerlike HRGOs/Ni-Doped MoS_2 Composite. *J. Alloys Compd.* **2020**, *824*, 153873. https://doi.org/10.1016/j.jallcom.2020.153873.

(17) Xue, Y.; Bai, X.; Xu, Y.; Yan, Q.; Zhu, M.; Zhu, K.; Ye, K.; Yan, J.; Cao, D.; Wang, G. Vertically Oriented Ni-Doped MoS2 Nanosheets Supported on Hollow Carbon Microtubes for Enhanced Hydrogen Evolution Reaction and Water Splitting. *Compos. Part B Eng.* **2021**, *224* (August). https://doi.org/10.1016/j.compositesb.2021.109229.

(18) Kong, X.; Wang, N.; Zhang, Q.; Liang, J.; Wang, M.; Wei, C.; Chen, X.; Zhao, Y.; Zhang, X. Ni-Doped MoS2 as an Efficient Catalyst for Electrochemical Hydrogen Evolution in Alkine Media. *ChemistrySelect*. 2018, pp 9493–9498. https://doi.org/10.1002/slct.201802100.

(19) Xue, Y.; Bai, X.; Xu, Y.; Yan, Q.; Zhu, M.; Zhu, K.; Ye, K.; Yan, J.; Cao, D.; Wang, G. Vertically Oriented Ni-Doped MoS_2 Nanosheets Supported on Hollow Carbon Microtubes for Enhanced Hydrogen Evolution Reaction and Water Splitting. *Compos. Part B Eng.* **2021**, *224* (August), 109229. https://doi.org/10.1016/j.compositesb.2021.109229.

(20) Zhou, X.; Xu, B.; Lin, Z.; Shu, D.; Ma, L. Hydrothermal Synthesis of Flower-Like MoS_2 Nanospheres for Electrochemical Supercapacitors. *J. Nanosci. Nanotechnol.* **2014**, *14* (9), 7250–7254. https://doi.org/10.1166/jnn.2014.8929.

(21) Chen, A. Y.; Liu, H. H.; Qi, P.; Xie, X. F.; Wang, M. T.; Wang, X. Y. Journal of Alloys and Compounds. *J. Alloys Compd.* **2021**, *864*, 158144. https://doi.org/10.1016/j.jallcom.2020.158144.

(22) Blöchl, P. E. Projector Augmented-Wave Method. *Phys. Rev. B* **1994**, *50* (24), 17953–17979. https://doi.org/10.1103/PhysRevB.50.17953.

(23) Perdew, J. P.; Burke, K.; Ernzerhof, M. Generalized Gradient Approximation Made Simple. *Phys. Rev. Lett.* **1996**, *77* (18), 3865–3868. https://doi.org/10.1103/PhysRevLett.77.3865.

(24) Kresse, G.; Furthmüller, J. Efficiency of Ab-Initio Total Energy Calculations for Metals and Semiconductors Using a Plane-Wave Basis Set. *Comput. Mater. Sci.* **1996**, *6* (1), 15–50. https://doi.org/10.1016/0927-0256(96)00008-0.

(25) Dion, M.; Rydberg, H.; Schröder, E.; Langreth, D. C.; Lundqvist, B. I. Van Der Waals Density Functional for General Geometries. *Phys. Rev. Lett.* **2004**, *92* (24), 246401. https://doi.org/10.1103/PhysRevLett.92.246401.

(26) Klimeš, J.; Bowler, D. R.; Michaelides, A. Chemical Accuracy for the van Der Waals Density Functional. *J. Phys. Condens. Matter* **2010**, *22* (2), 022201. https://doi.org/10.1088/0953-8984/22/2/022201.

(27) Klimeš, J.; Bowler, D. R.; Michaelides, A. Van Der Waals Density Functionals Applied to

Solids. *Phys. Rev. B* **2011**, *83* (19), 195131. https://doi.org/10.1103/PhysRevB.83.195131.

(28) Hlova, I. Z.; Singh, P.; Malynych, S. Z.; Gamernyk, R. V.; Dolotko, O.; Pecharsky, V. K.; Johnson, D. D.; Arroyave, R.; Pathak, A. K.; Balema, V. P. Incommensurate Transition-Metal Dichalcogenides via Mechanochemical Reshuffling of Binary Precursors. *Nanoscale Adv.* **2021**, *3* (14), 4065–4071. https://doi.org/10.1039/D1NA00064K.

(29) Dolotko, O.; Hlova, I. Z.; Pathak, A. K.; Mudryk, Y.; Pecharsky, V. K.; Singh, P.; Johnson, D. D.; Boote, B. W.; Li, J.; Smith, E. A.; et al. Unprecedented Generation of 3D Heterostructures by Mechanochemical Disassembly and Re-Ordering of Incommensurate Metal Chalcogenides. *Nat. Commun.* **2020**, *11* (1), 3005. https://doi.org/10.1038/s41467-020-16672-0.

(30) Lai, W.; Chen, Z.; Zhu, J.; Yang, L.; Zheng, J.; Yi, X.; Fang, W. A NiMoS Flower-like Structure with Self-Assembled Nanosheets as High-Performance Hydrodesulfurization Catalysts. *Nanoscale* **2016**, *8* (6), 3823–3833. https://doi.org/10.1039/c5nr08841k.

(31) Fei, L.; Lei, S.; Zhang, W.-B.; Lu, W.; Lin, Z.; Lam, C. H.; Chai, Y.; Wang, Y. Direct TEM Observations of Growth Mechanisms of Two-Dimensional MoS_2 Flakes. *Nat. Commun.* **2016**, *7* (1), 12206. https://doi.org/10.1038/ncomms12206.

(32) Wang, D.; Zhang, X.; Shen, Y.; Wu, Z. Ni-Doped MoS 2 Nanoparticles as Highly Active Hydrogen Evolution Electrocatalysts. *RSC Adv.* **2016**, *6* (20), 16656–16661. https://doi.org/10.1039/C6RA02610A.

(33) Luo, R.; Luo, M.; Wang, Z.; Liu, P.; Song, S.; Wang, X.; Chen, M. The Atomic Origin of Nickel-Doping-Induced Catalytic Enhancement in MoS_2 for Electrochemical Hydrogen Production. *Nanoscale* **2019**, *11* (15), 7123–7128. https://doi.org/10.1039/C8NR10023C.

(34) Ghosh, S.; Samanta, P.; Jang, W.; Yang, C.-M.; Murmu, N. C.; Kuila, T. Improvement of the Supercapacitor Performance of Nickel Molybdenum Chalcogenides/Reduced Graphene Oxide Composites through Vanadium-Doping Induced Crystal Strain Relaxation and Band Gap Modification. *ACS Appl. Energy Mater.* **2022**, *5* (2), 1528–1541. https://doi.org/10.1021/acsaem.1c02932.

(35) Escalera-López, D.; Niu, Y.; Yin, J.; Cooke, K.; Rees, N. V.; Palmer, R. E. Enhancement of the Hydrogen Evolution Reaction from Ni-MoS_2 Hybrid Nanoclusters. *ACS Catal.* **2016**, *6* (9), 6008–6017. https://doi.org/10.1021/acscatal.6b01274.

(36) Gómez-Balderas, R.; Martínez-Magadán, J. M.; Santamaria, R.; Amador, C. Promotional Effect of Co or Ni Impurity in the Catalytic Activity of MoS_2: An Electronic Structure Study. *Int. J. Quantum Chem.* **2000**, *80* (3), 406–415. https://doi.org/10.1002/1097-461X(2000)80:3<406::AID-QUA10>3.3.CO;2-2.

(37) Najib, S.; Erdem, E. Current Progress Achieved in Novel Materials for Supercapacitor Electrodes: Mini Review. *Nanoscale Adv.* **2019**, *1* (8), 2817–2827. https://doi.org/10.1039/c9na00345b.